Proceedings of the ASME 2010 3rd Joint US-European Fluids Engineering Summer Meeting and 8th International Conference on Nanochannels, Microchannels, and Minichannels
FEDSM-ICNMM2010
August 1-5, 2010, Montreal, Canada

FEDSM-ICNMM2010-30898

COMPUTATIONAL FLUID-STRUCTURE INTERACTION OF DGB PARACHUTES IN COMPRESSIBLE FLUID FLOW

Carlos Pantano-Rubino
Department of Mechanical and Science Engineering
University of Illinois
1206 West Green Street
Urbana, Illinois, USA, 61801
cpantano@illinois.edu

Kostas Karagiozis
Department of Mechanical Engineering
McGill University
817 Sherbrooke Street West
Montreal, Quebec, Canada, H3A 2K6
konstantinos.karagiozis@mcgill.ca

Ramji Kamakoti
Department of Mechanical and Science Engineering
University of Illinois
1206 West Green Street
Urbana, Illinois, USA 61801
cpantano@illinois.edu

Fehmi Cirak
Department of Engineering
University of Cambridge
Trumpington Street
Cambridge, UK, CB2 1PZ
fc286@eng.cam.ac.uk

ABSTRACT
This paper describes large-scale simulations of compressible flows over a supersonic disk-gap-band parachute system. An adaptive mesh refinement method is used to resolve the coupled fluid-structure model. The fluid model employs large-eddy simulation to describe the turbulent wakes appearing upstream and downstream of the parachute canopy and the structural model employed a thin-shell finite element solver that allows large canopy deformations by using subdivision finite elements. The fluid-structure interaction is described by a variant of the Ghost-Fluid method. The simulation was carried out at Mach number 1.96 where strong nonlinear coupling between the system of bow shocks, turbulent wake and canopy is observed. It was found that the canopy oscillations were characterized by a breathing type motion due to the strong interaction of the turbulent wake and bow shock upstream of the flexible canopy.

1. INTRODUCTION
Supersonic parachutes have been used as aerodynamic decelerators during entry and decent into low-density atmospheres, e.g., exploration mission to Mars. The deployment of such parachutes, at supersonic speeds, involves complex fluid structure interaction (FSI) phenomena. It is evident that the rapid change of the parachute shape greatly affects the parachute stability and deceleration rate. It involves the inevitable coupling between parachute and flow (strongly coupled highly nonlinear fluid-structure interaction), bluff body (flow-induced vibrations-FIV) and porous aerodynamics due to shape and size of the parachute, complex dynamics associated with an axial movement of the bow shock upstream of the canopy due to over-under pressurization, random loading due to the movement of the suspension lines that connect the parachute with the capsule (entry vehicle), contact forces due to the folding of the parachute and inflation instabilities due to the imbalance of fluid forces and parachute inertia with the internal and cable (suspension lines) forces. The FSI and FIV phenomena become even more complicated if the turbulent wake generated by the upstream payload is considered in the analysis. Hence, the performance and efficiency of a supersonic parachute is a function of the shape and design of the

parachute, Mach number, wake behind the parachute and the capsule, upstream bow-shock dynamics, fluid properties, landing altitude and location (distance from equator) and size and weight of capsule.

By late 1950's experimental work on the use of parachutes for spacecraft applications had already started producing results for specific parachute designs. One of the first complete studies on the aerodynamics of supersonic decelerators is the work by Maynard [1] examining the aerodynamic characteristics of different types of supersonic decelerators including the effect of balloons, drag chutes, paragliders, and parachutes. A 40-ft nominal diameter disk-gap-band (DGB) parachute was investigated in an analytical and experimental study calculating estimates of maximum expected loads, proposing different parachute configurations, preparing a stress analysis, defining moments of inertia, and collecting component structural data [2]. Research on the performance of DGB parachutes had become a priority by mid 1960s. The DGB parachute had been originally designed to be used as a decelerator for high-altitude meteorological rocket systems [3]. NASA conducted large-scale experiments investigating the performance of a 30-ft diameter DGB parachute in flight tests [4]. The test was performed using a rocket launch method. The parachute was deployed at Mach number 1.56 and a dynamic pressure of 11 $[\mathrm{lb/ft^2}]$ (546 $[\mathrm{N/m^2}]$) at an altitude of 127,500 feet or 38.86 km. Continuous oscillations of the canopy was observed almost immediately after deployment. When the parachute was fully inflated (in less than 1 second) the total load was 3915 pounds (17,400 N). The parachute exhibited an average drag coefficient of 0.52 and pitch-yaw oscillations of 5° or less. During the steady-state descent the average drag coefficient dropped to 0.47. A comparison study based on flight-test experiments on the performance of modified-ringsail, disk-gap-band and cross parachute systems was conducted by Whitlock et al. [5]. The deployment of the parachutes was performed under simulated Martian environmental conditions. It was found that canopy stability was acceptable for Mach numbers lower than 1.4 for the modified-ringsail and DGB parachutes. It is important to note that for higher Mach numbers some tests for DGB and ringsail parachutes indicated large-amplitude canopy oscillations and that the cross-parachute configurations were unstable throughout the experiments even though they achieved the highest drag coefficient values with the ringsail obtaining the second largest values for the drag coefficient.

Another experimental study was performed at Langley's 4-foot wind tunnel to determine the effects of variation in reefing ratio and geometric porosity on the drag and stability characteristics of cross, hemiflo, DGB and extended-skirt parachutes at Mach number 1.80 [6]. In addition, modular cross and standard flat canopies and a ballute were also investigated. It was found that cross parachutes were the most unstable with drag variations due to breathing and squidding on the canopy and coning motions of the parachute. Based on the results from the wind tunnel an empirical correlation for the drag coefficients in transonic and supersonic flows for parachutes with specific porosity and reefing ratio was developed and it was concluded that reefing ratio, geometric porosity and Mach number are the most significant parameters in estimating the drag coefficient, which is in agreement with the results obtained by [7].

Lingard and Darley [8] presented a fully coupled fluid-structure interaction model using the Arbitrary Lagrangian Euler methodology for simulating the flexible parachute incorporated with the commercial code LS-DYNA used to describe the flow conditions at Mach 1.5. Results for the flow field are in qualitative agreement with experimental results available in the literature.

NASA continued its experimental testing of DGB supersonic parachutes at high Mach numbers. In a recent study described in Sengupta et al. [9] a 0.813 m DGB parachute was subjected to supersonic flow and wake produced by a Viking-type entry vehicle at NASA's Glenn Research Center (GRC) 10'x10' wind-tunnel. The Mach number reached values up to 2.5 and the Reynolds number was $3\mathrm{x}10^6$, which is representative of the Mars Science Laboratory (MSL) mission flow conditions. The parachute itself was a 4% scaled down MSL parachute and was attached to a 4% scale Viking-heritage entry-vehicle also designed for the same mission. Two different configurations, one unconstrained and the other with constraints allowing translation of the parachute only along the axial direction were investigated. In-line load cells and high speed cameras recorded measurements for the unsteady and mean drag coefficients as a function of Mach and Reynolds numbers, supersonic inflation, parachute trim angle, projected area and frequency of area oscillations. A brief description of the parachute deployment sequence for the MSL DGB supersonic decelerator is also found in [10]. In a more recent report by Sengupta et al. [11] a detailed discussion on the experimental and theoretical findings for the supersonic qualification program of the MSL parachute system is presented. They discussed the difficulties and uniqueness of the MSL mission compared to other past missions to Mars. They noted that for this mission the supersonic DGB parachute will spend up to 10 seconds above Mach 1.5 which is the threshold for increased amplitude area oscillations (Refs. [5,12,13]). They present a new CFD model that utilizes a large-eddy simulation approach to investigate the wake of the MSL capsule upstream of the parachute and the wake and its effect generated downstream of the parachute. They also presented a set of experiments for a 4% scaled down parachute system. Preliminary results from the new CFD model for rigid parachutes were shown to be in good quantitative and qualitative agreement with the experimental results.

In this paper a new theoretical computational fluid dynamics (CFD) study is presented, investigating the fluid-structure interaction between the MSL DGB parachute and supersonic flow. The computational approach utilizes structured adaptive mesh refinement, large-eddy simulation to describe the turbu lent flow and a finite-element method utilizing subdivision elements to describe the parachute motion.

The fluid-structure interaction is modeled using a variant of the Ghost-Fluid method.

2. THEORY

A typical configuration of a supersonic parachute along with the payload is shown in Fig.1. It consists of a capsule (payload), the disk-gap-band supersonic parachute and the cables connecting the payload with the parachute. The reference coordinate system is centered at the plane of maximum diameter of the capsule with its *x*-coordinate aligned with the mean flow direction, as shown. The capsule is fixed at point A while the canopy and cables are free to move due to their interaction with the supersonic fluid. The distance between the origin of the coordinate system of reference and the parachute is H=1.824 m. The connecting cables are anchored at point B with coordinates x_B=35.4 cm. The parachute and its cables are connected using the patterns discussed in Reuter et al. [14]. The capsule geometry is scaled down from the Viking mission capsule (70^0 sphere-cone entry vehicle). The capsule dimensions are: d=16.96 cm with w=10.72 cm. The dimensions of the parachute are: D=55.88 cm, D_0=9.3 cm, L_B=10.16 cm, and L_G=10.16 cm. For this study H/d=10.75. In addition, the Mach number considered in this analysis was set to 1.96.

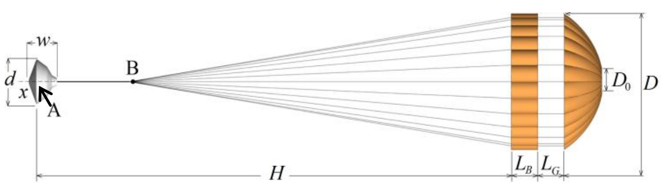

FIGURE 1. Configuration of a disk-gap-band supersonic parachute and its payload.

2.1 Fluid model

Assuming negligible viscous work and triple correlations, the large-eddy simulation (LES) dimensional conservation transport equations for the conservation of mass, momentum and total energy of the fluid based on the Favre-filtered (i.e. density weighted) quantities [15], denoted with overbars, are given by

$$\partial\bar{\rho}/\partial t + \partial\bar{\rho}\tilde{u}_j/\partial x_j = 0\,,$$
$$\partial\bar{\rho}\tilde{u}_i/\partial t + \partial\left(\bar{\rho}\tilde{u}_i\tilde{u}_j + \bar{p}\delta_{ij}\right)/\partial x_j = \partial\sigma_{ij}/\partial x_j - \partial\tau_{ij}/\partial x_j\,,$$
$$\partial\bar{E}/\partial t + \partial\left(\bar{E}+\bar{p}\right)\tilde{u}_j/\partial x_j = \partial\left(\bar{\kappa}\partial\bar{T}/\partial x_j\right)/\partial x_j + \partial\sigma_{ji}\tilde{u}_i/\partial x_j - \partial q_j^T/\partial x_j\,, \quad (1)$$

where $\bar{\rho}$ is the density, $\bar{\rho}\tilde{u}_i$ is the fluid momentum, $\bar{p}$ is the pressure (determined by the ideal gas equation of state), δ_{ij} is Kronecker's delta, σ_{ij} is the Newtonian stress tensor defined by $\sigma_{ij} = \bar{\mu}\left\lfloor\left(\partial\tilde{u}_i/\partial x_j + \partial\tilde{u}_j/\partial x_i\right) - \left(2\partial\tilde{u}_k/3\partial x_k\right)\delta_{ij}\right\rfloor$, $\bar{\mu}$ is the Favre-filtered value for the viscosity, $\bar{\kappa}$ is the heat conductivity coefficient, $\bar{T}$ is the Favre-filtered temperature, $\tau_{ij} = \bar{\rho}\left(\widetilde{u_i u_j} - \tilde{u}_i\tilde{u}_j\right)$, $q_j^T = \rho\left(\widetilde{c_p T u_j} - \tilde{c}_p\tilde{T}\tilde{u}_j\right)$, and $\bar{E}$ is the filtered total energy given by

$$\bar{E} = \frac{\bar{p}}{(\tilde{\gamma}-1)} + \frac{1}{2}\bar{\rho}\left(\tilde{u}_k\tilde{u}_k\right) + \frac{1}{2}\tau_{kk}\,, \quad (2)$$

where $\tilde{\gamma} = \tilde{c}_p/\tilde{c}_v$ is the average specific heat ratio, $\tilde{c}_p$ is the specific heat capacity at constant pressure and $\tilde{c}_v$ is the specific heat capacity at constant volume.

Furthermore, closure to LES equations is achieved in the form of a model for subgrid quantities [16]. The subgrid stress tensor τ_{ij} and the turbulent temperature flux q_i^T are computed using the stretched-vortex subgrid-scale model for compressible and subgrid scalar transport flows [17, 18]. The resulting subgrid stresses are

$$\tau_{ij} = \bar{\rho}\tilde{k}\left(\delta_{ij} - e_i^v e_j^v\right), \quad (3)$$

$$q_i^T = -\bar{\rho}\frac{\Delta_c}{2}\tilde{k}^{1/2}\left(\delta_{ij} - e_i^v e_j^v\right)\frac{\partial\left(\tilde{c}_p\tilde{T}\right)}{\partial x_j}, \quad (4)$$

where

$$\tilde{k} = \int_{k_c}^{\infty} E(k)\,dk\,, \quad (5)$$

is the subgrid energy, $\mathbf{e}^{\mathbf{v}}$ is the unit vector aligned with the subgrid vortex axis, $k_c = \pi/\Delta_c$ is the largest resolved wavenumber, and Δ_c is taken to be the grid spacing. The subgrid turbulent kinetic energy is estimated using the spiral vortex assumption by [19] whose energy (velocity) spectrum for the subgrid motion is given by

$$E(k) = K_0\varepsilon^{2/3}k^{-5/3}\exp\left[-2k^2\nu/2|\tilde{a}|\right], \quad (6)$$

where K_0 is the Kolmogorov prefactor, ε is the local cell averaged dissipation and $\tilde{a} = \tilde{S}_{ij}e_i^v e_j^v$ is the axial strain along the subgrid vortex axis with a resolved rate of strain tensor given by

$$\tilde{S}_{ij} = \frac{1}{2}\left(\frac{\partial\tilde{u}_i}{\partial x_j} + \frac{\partial\tilde{u}_j}{\partial x_i}\right). \quad (7)$$

Furthermore, the group prefactor $K_0\varepsilon^{2/3}$ is refined from the resolved flow [18, 20, 21] using the following expression

$$K_0\varepsilon^{2/3} = \frac{\bar{F}_2(\Delta)}{\Delta^{2/3}A}\,, \quad (8)$$

where $A = 4\int_0^{\pi} s^{-5/3}\left(1 - s^{-1}\sin s\right)ds \approx 1.90695$, and

$$\bar{F}_2(\Delta)=\frac{1}{6}\sum_{j=1}^{3}\left(\delta\tilde{u}_1^{+2}+\delta\tilde{u}_2^{+2}+\delta\tilde{u}_3^{+2}+\delta\tilde{u}_1^{-2}+\delta\tilde{u}_2^{-2}+\delta\tilde{u}_3^{-2}\right)_j, \quad (9)$$

where $\delta\tilde{u}_i^{\pm}=\tilde{u}_i\left(\mathbf{x}_0\pm\mathbf{e}_j\Delta\right)-\tilde{u}_i\left(\mathbf{x}_0\right)$ denotes the ith velocity component difference in the unitary direction $\mathbf{e}_j$ and $\mathbf{x}_0$. Appropriately resolving the energy-containing velocity spectrum (keeping the subgrid energy contribution small) enables modeling of turbulence amplification as it traverses shocks. It is expected that the shock-turbulence interaction modeling uncertainties will be small, at least when few interactions are present, as in the present case.

2.2 Thin shell model

The parachute is modeled using a thin-shell theory including the membrane and bending energies. A Lagrangian description is used and the equilibrium equation in the weak form is given by

$$G_{\text{dyn}}+G_{\text{int}}-G_{\text{ext}}=0. \quad (10)$$

The first term represents the contribution of the inertial forces given by

$$G_{dyn}=\int_{\bar{\Omega}}\rho_s\ddot{\mathbf{x}}\delta\mathbf{x}\, d\bar{\Omega}, \quad (11)$$

where ρ_s is the mass density of the structure, $\ddot{\mathbf{x}}$ is the acceleration of the mid surface, $\delta\mathbf{x}$ are virtual deformations, and $\bar{\Omega}$ is the reference shell mid-surface (integration domain). The rotational inertia terms are neglected since their contribution is expected to be small for thin shells. The second term in Eq. (10) denotes all the internal forces from the membrane and bending energies and is given by

$$G_{\text{int}}=\int_{\bar{\Omega}}\mathbf{n}\delta\boldsymbol{\alpha}\, d\bar{\Omega}+\int_{\bar{\Omega}}\mathbf{m}\delta\boldsymbol{\beta}\, d\bar{\Omega}, \quad (12)$$

where $\mathbf{n}$ is the stress resultant tensor, $\boldsymbol{\alpha}$ is the conjugate strain tensor, $\mathbf{m}$ is the moment resultant and $\boldsymbol{\beta}$ is the respective conjugate strain tensor. The last term in Eq. (10) represents the external force (pressure by the fluid) given by

$$G_{\text{ext}}=\int_{\bar{\Omega}}p\mathbf{d}\delta\mathbf{x}\, d\bar{\Omega}, \quad (13)$$

where p is the pressure exerted by the fluid. The direction of the pressure loading is always in the direction of the shell normal $\mathbf{d}$ and orthogonal to the mid-surface.

Subdivision elements [22] are used for discretizing the equilibrium equations in weak form. The final discrete equation of motion is given by

$$\mathbf{M}\ddot{\mathbf{x}}_h+\mathbf{f}_{\text{int}}\left(\mathbf{x}_h\right)-\mathbf{f}_{\text{ext}}\left(\mathbf{x}_h,t\right)=0, \quad (14)$$

where $\mathbf{M}$ is the mass matrix, $\ddot{\mathbf{x}}_h$ is the acceleration vector, and $\mathbf{f}_{\text{int}}$ and $\mathbf{f}_{\text{ext}}$ are the internal and external force vectors, respectively. The equations of motion are integrated over time using the explicit Newmark scheme. The critical time step used in the integration of the structure is usually smaller than the critical step in the fluid solver (since the structure tends to be more stiff than the fluid) and a subcycling technique is employed to integrate the overall equations in time.

2.3 Fluid-structure interaction modeling

The computational fluid dynamics and finite element analysis models interact only in a thin region around the interface boundary using a temporal splitting method (which is appropriate for compressible flows). This interaction is modeled using a variant of the Ghost-Fluid Method (GFM) [23]. All the fluid cells that are overlapped by the structural elements are reconstructed by identical cells within the solid elements that satisfy approximately the boundary conditions at the interface between fluid and solid. These reconstructed cells are referred to as the *ghost cells*. The solid boundary in the Cartesian fluid solver is represented by a level set technique [24, 25]. The boundary conditions for the transmural pressure and flow velocity at the interface are then applied on the ghost cells.

The resulting force from the fluid-structure interaction acting at the interface boundary is given by

$$\mathbf{f}^{\text{ext}}=\bar{p}\,\mathbf{d}\big|_{\Gamma^+\cup\Gamma^-}, \quad (15)$$

where Γ^+ and Γ^- denote the limit surfaces that approach the shell mid-surface Γ from both solid and fluid sides. The normal to surfaces, $\mathbf{d}$, is taken to be positive outwards from the fluid region. Essentially, equation (15) represents the transmural pressure (difference of pressure across the surface) at the fluid-structure interface.

The slip boundary condition for the fluid and zero normal pressure and density gradients are used for the mass and energy conservations equations for reflective wall-boundary conditions in the inviscid approximation [26].

3. NUMERICAL RESULTS

The flow conditions used in the numerical experiment presented in this study are shown in Table 1.

M	Re	q (Pa)	u_∞ (m/s)	$\Delta_{\min}$ (mm)
1.96	122,143	4202.5	674.9	3.9

Table 1: Flow conditions used in the simulation.

The parameters in Table 1 are defined as: Mach number $M=u_\infty/c_\infty$, dynamic pressure $q=1/2\,\rho_\infty u_\infty^2$, where u_∞, ρ_∞, and c_∞ are the free-stream velocity, density and speed of sound, respectively. The Reynolds number, Re, is defined using the capsule diameter according to $\mathrm{Re} = \rho_\infty u_\infty d/\mu_\infty$, where μ_∞ denotes the dynamic viscosity at the conditions of the flow upstream. The supersonic parachute has a Young's Modulus E=878 MPa, Poisson's ratio v=0.33, thickness h=0.0635 mm and mass density $\rho_s = 614$ kg/m^3. The cables have an elastic modulus E=43 GPa and their density per unit area is $\rho_c = 8.27\ 10^{-4}$ kg/m with a diameter $\phi = 0.495$ mm. The flow conditions and material properties used in this simulation match those used in the experimental study by [26].

The computational domain is $[3,5]\times[-1,1]\times[-1,1]$ (meters) with the capsule centered at the origin. The coarse mesh resolution based on the AMR level is $\Delta x = \Delta y = \Delta z = 1/32$ m. In our case three additional levels of refinement were used to increase resolution appropriately within the AMR framework (usually around shocks, interface boundary, and turbulent wakes). The total number of grid cells in the simulation varied with time ranging from 12 to 50 million. The simulation was run on a SGI Altix 3700 System at the Supercomputer and Visualization Facility at the Jet Propulsion Laboratory. It utilized 100 processors (96 assigned to the fluid and 4 to the structure) and required approximately 4 months to complete the run.

3.1 Fluid dynamics

Figure 2 shows the compressible flow around the supersonic parachute decomposed into a number of canonical regions. The capsule, canopy and suspension lines as well as color iso-contour levels of the streamwise velocity, $\tilde{u}$, and iso-lines of pressure (shown with black colored lines) at t=57.5 ms are shown in the central plane of the computational domain.

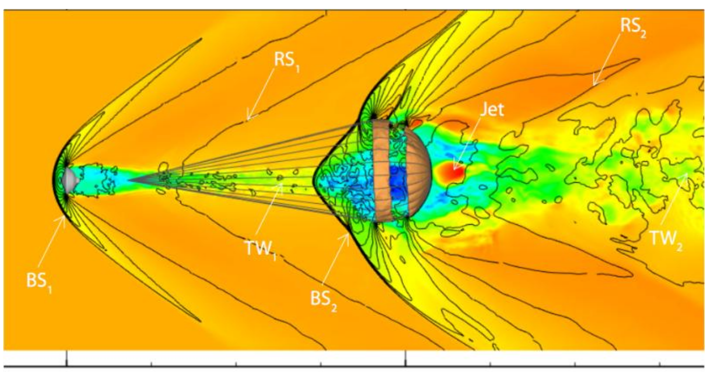

FIGURE 2. General flow features around the capsule and flexible supersonic canopy. Iso-contours indicate velocity and isolines denote the pressure for t=57.5 ms.

There are two bow shocks, BS$_1$ and BS$_2$, ahead of the capsule and canopy, respectively. These shocks influence the supersonic conditions upstream of the rigid capsule boundary and flexible canopy. A stable narrow turbulent wake, TW$_1$, develops behind the rigid capsule (which is fixed in space) and a rather unsteady irregular turbulent wake, TW$_2$, develops behind the deformed canopy. Two recompression shocks, RS$_1$ and RS$_2$, are seen behind the capsule and canopy due to the detached flow in these regions. Moreover, a supersonic jet also develops from the hole of the canopy.

It was observed that a breathing response was developed in time due to the interaction of the bow shock and irregularities of the turbulent wake TW$_1$. This interaction gives rise to transmural pressure fluctuations forcing large-amplitude parachute oscillations that augment the unsteadiness of the bow shock BS$_2$ and initiate the canopy breathing movement.

3.2 Canopy dynamics

The flexible canopy oscillates in a breathing fashion due to the interaction of the bow shock BS$_2$ with the turbulent wake TW$_1$ and the structure. Figure 3 shows different canopy configurations within a cycle of oscillation.

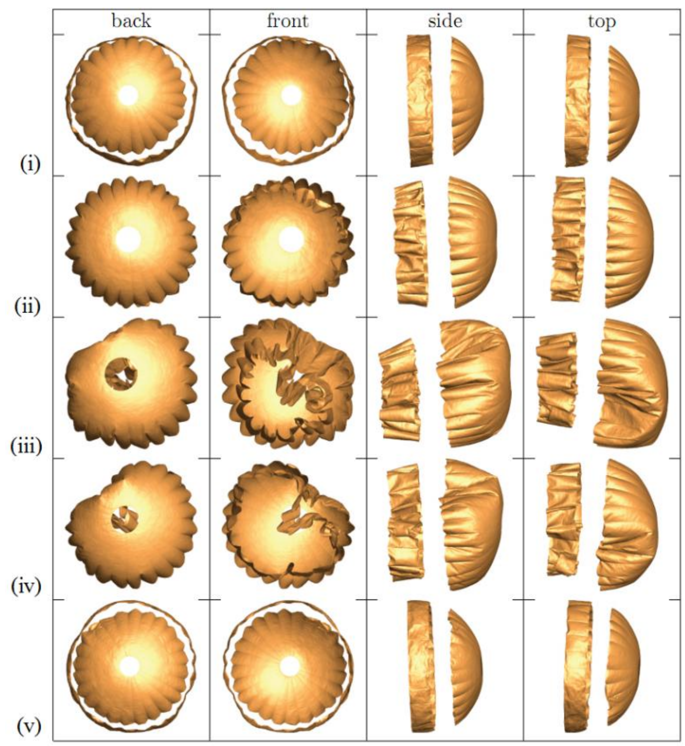

FIGURE 3. Canopy breathing cycle.

In stage (i) the canopy is fully inflated with small deformations mostly in the radial direction of the parachute. In stage (ii) the band shows large deformations mostly due to the cable forces. Clearly, in stage (iii) the parachute is partially collapsed with large amplitude deformations. It is interesting that the collapse is not symmetrical and that it is strongly affected by the forces exerted by the cables on the canopy. It seems that the nonlinear oscillation of the parachute is more complex as the wake generated behind the canopy enhances a non-symmetrical partial collapse of the parachute favoring only one side of the canopy. In stage (iv) the parachute is slowly inflated again and in stage (v) the canopy is fully opened. A similar partial collapse of the canopy was observed in the experimental work by [27]. This deflation-inflation cycle of the nominal parachute area is shown in Fig. 4 as a plot of the ratio of the instantaneous projected canopy frontal area over the original frontal area, $S_0 = \pi D^2/4$, versus time.

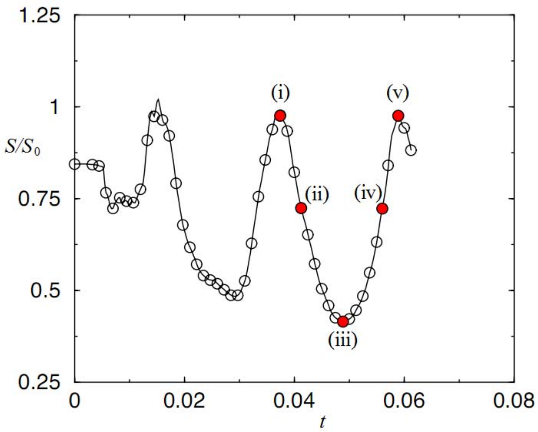

FIGURE 4. Cyclical frontal canopy area fluctuation over time.

3.3 Pressure dynamics

It was found that the drag force on the rigid capsule remained insensitive to the dynamics of the canopy. The reason is that the bow shock upstream of the capsule is very stable and not easily perturbed by the turbulent wake behind the capsule. The capsule drag is steady and varies less than 1% during the simulation time. The drag force on the canopy changes dynamically due to the multiple interactions of the turbulent wake behind the canopy, the bow shock unsteadiness and the induced large canopy deformation. However, after the initial transient, the drag attains an almost periodic cycle (the breathing movement of the parachute). Table 2 gives the simulation results for the average drag forces over one breathing cycle applied on the capsule, F_c, and parachute, F_p and their corresponding drag coefficients C_c and C_p, respectively.

F_c (N)	F_p (N)	C_c	C_p
130	717	1.37	0.34

Table 2: Force distribution on the canopy and parachute.

4. CONCLUSIONS

This paper summarizes some results of a simulation of the complex dynamical behaviour of a disk-gap-band parachute connected to a rigid capsule in supersonic flow. The coupled model utilized adaptive mesh refinement using large-eddy simulation for compressible flows and a thin-shell solver with subdivision finite elements to describe the large oscillations of DGB parachutes. It was found that high Mach number flows destabilize the parachute due to the strong interaction of the turbulent wake of the upstream capsule and the dynamics of the bow shock appearing before the canopy. The dynamics of the interaction of the turbulent flow and thin structure generate a breathing type parachute oscillation with very large deformations and rapid changes in the canopy drag coefficient, in agreement with experimental observations. These oscillations degrade the overall performance of the supersonic decelerator.

ACKNOWLEDGEMENT

This work was supported by the Jet Propulsion Laboratory under contract 1291711 with the California Institute of Technology (technical program manager Dr. A. Sengupta). The authors would also like to thank Prof. P.E. Dimotakis for introducing them to the flow-physics of supersonic parachutes.

REFERENCES

[1] Maynard, J.D., 1960, "Aerodynamics of decelerators at supersonic speeds", In Proceedings: AIAA Proceedings of the Recovery of Space Vehicles Symposium, pp. 48-54.

[2] Lemke, R., 1967. Final Report – 40 ft DGB parachute. Presented to Martin Marietta, Dernver, Colorado (NASA CR-66587).

[3] Eckstrom, C.V., 1966. Development and testing of the disk-gap-band parachute used for low dynamic pressure applications at ejection altitudes at or above 200,000 feet. NASA CR-502.

[4] Eckstrom, C.V., Preisser, J.S., 1967. Flight test of a 30-foot-nominal-diameter disk-gap-band parachute deployed at a Mach number of 1.56 and a dynamic pressure of 11.4 pounds per square foot. NASA Technical Memorandum TM X-1451.

[5] Whitlock, C.H., Bendura, R.J., 1969. Inflation and performance of three parachute configurations from supersonic test in a low-density environment. NASA Technical Note, D-5296.

[6] Couch, L.M., 1975. Drag and stability characteristics of a variety of reefed and unreefed parachute configurations at Mach 1.80 with an empirical correlation for supersonic Mach numbers. NASA Technical Report R-429.

[7] Johnson, C.T., 1960. Investigation of the characteristics of 6-foot drogue-stabilization ribbon parachutes at high altitudes and low supersonic speeds. NASA Technical Memorandum, X-448.

[8] Lingard, J.S., Darley, M.G., 2005. "Simulation of parachute fluid structure interaction in supersonic flow". In Proceedings: 18th AIAA Aerodynamic Decelerator Systems Technology Conference and Seminar, May 23-25, Munich, Germany (AIAA-2005-1607).

[9] Sengupta, A., Roeder, J., Kelsch, R., Wernet, M., Kandis, M., Witkowski, A., 2008. Supersonic disk gap band parachute performance in the wake of a Viking-type entry vehicle from Mach 2 to 2.5. In Proceedings: AIAA Atmospheric Fligh Mechanics Conference and Exhibit, August 18-21, Honolulu, Hawaii (AIAA-2008-6217).

[10] Birge,III, B.K., 2008. *A computational intelligence approach to the Mars precision landing problem*. PhD Thesis, North Carolina State University, Raleigh, North Carolina.

[11] Sengupta, A., Steltzner, A., Witkowski, A., 2009. Findings from the supersonic qualification program of the Mars science laboratory parachute system. In Proceedings: 20th AIAA Aerodynamic Decelerator Systems Technology Conference and Seminar, 4-7 May, Seattle, Washnigton (AIAA-2009-2900).

[12] Steinberg, S., Siemers III, P.M., Slayman, R.G., 1974. "Development of the Viking parachute configuration by wind-tunnel investigation". Journal of Spacecraft, **11**, pp. 101-107.

[13] Way, D.W., Powell, R.W., Chen, A., Steltzner, A.D., San Martin, A.M., Burkhart, P.D., Mendeck, G.F., 2006. Mars Science Laboratory: Entry, descent, and landing system performance. In Proceedings: IEEE, Aerospace Conference (#1467), March 3-10, Big Sky, Montana.

[14] Reuter, J., Machalik, W., Witkowski, A., Kandis, M., Sengupta, A., Kelsch, R., 2009. Design of suitable parachute models for MSL supersonic wind tunnel testing. In Proceedings: 20th AIAA Aerodynamic Deceleraotr Systems Technology Conference and Seminar. No. 2999-569. Seattle, Washington.

[15] Zang, T.A., Dahlburg, R.B., Dahlburg, J.P., 1992. "Direct and large-eddy simulations of 3-dimensional compressible navier-stokes urbulence". *Phys Fluids A – Fluid Dynam*, **4**, pp. 127-140.

[16] Pope, S.B., 2004. Ten questions concerning the large-eddy simulation of turbulent flows". *New Journal of Physics*, **6**, Art. 35.

[17] Kosovic, B., Pullin, D.I., Smtaney, R., 2002. "Subgrid-scale modeling for large-eddy simulations of compressible turbulence". *Phys. Fluids*, **14**, pp. 1511-1522.

[18] Pullin, D.I., 2004. "A vortex-based model for the subgrid flux of a passive scalar". *Phys. Fluids*, **12**, pp. 2311-2319.

[19] Lundgren, T.S., 1982. "Strained spiral vortex model for turbulent fine-structure". *Phys. Fluids*, **25**, pp. 2193-2203.

[20] Lesieur, M., Metais, O., 1996. New trends in large-eddy simulations of turbulence". *Annu. Rev. Fluid Mech.*, **28**, pp. 45-82.

[21] Voelkl, T., Pullin, D.I., Chan, D.C., 2000. "A physical-space version of the stretched-vortex subgrid-stress model for large-eddy simulation". *Phys. Fluids*, **12**, pp. 1810-1825.

[22] Cirak, F., Ortiz, M., Schröder, P., 2000. "Subdivision surfaces: a new paradigm for thin-shell time-element analysis". *Int. J., Numer. Meth. Eng.*, **47**, pp. 2039-2072.

[23] Fedkiw, R., Aslam, T., Merriman, B., Osher, S., 1999. "A non-oscillatory Elerian approach to interfaces in multimaterial flows (the ghost fluid method)". *J. Comput. Phys.*, **152**, pp. 457-492.

[24] Cirak, F., Deiterding, R., Mauch, S., 2006. "Large-scale fluid-structure interaction simulation of viscoplastic and fracturing thin shells subjected to shocks and detonations". *Computers and Structures*, **85**, pp. 1049-1065.

[25] Deiterding, R., Radovitzky, R., Mauch, S., Noels, L., Cummings, J., Meiron, D., 2006. A virtual test facility for the efficient simulation of solid materials under high-energy shock-wave loading". *Engineering with Computers*, **22**, pp. 325-347.

[26] Whitham, G., 1999. *Linear and nonlinear waves*. Wiley-Interscience.

[27] Sengupta, A., Wernet, M., Roeder, J., Kelsch, R., Witkowski, A., Jones, T., 2009. Supersonic testing of 0.8m disk gap parachutes in the wake of a 70 deg sphere cone entry vehicle. In Proceedings: 20th AIAA Aerodynamic Decelerator Systems Technology Conference and Seminar, Seattle, Washington.

[28] Eckstrom, C., 1970. Flight test of a 40-foot-nominal-diameter disk-gap-band parachute deployed at a amAch number of 1.56 and a dynamic pressure of 11.4 pounds per square foot. NASA Technical Report, TM X-1451.